Modeling and Optimized Design of the Free-Standing Magnetic Field Energy Harvester Based on Accurate Estimation of Effective Permeability

Zhu Liu, Likai Zheng, Siyu Bao, Aijun Yang, *Senior Member, IEEE*, Dan Zhou, Jifeng Chu, Huan Yuan, Mingzhe Rong, *Senior Member, IEEE*, and Xiaohua Wang, *Senior Member, IEEE*

***Abstract*—Free-standing magnetic field energy harvesters (FSMFEHs) offer a novel approach for powering sensors in the power IoT. A mathematical model is established in this article to provide a generalized design tool for the FSMFEH. An accurate estimation method for the effective permeability of the H-shaped core is proposed based on the effective permeability of the cylindrical core and flux continuity theorem, along with a correction term, to enhance the model's accuracy. Experimental results show that estimation errors are less than 8%. Based on this model, an effective performance optimization method for the FSMFEH is summarized. Especially, the differences in maximum power and maximum power density, and the impact of induced voltage on the power management circuit, are considered. In addition, utilizing the Steinmetz equation, it is found that the magnetic field generated by the coil current, rather than the external magnetic field, is the predominant factor leading to core losses. The optimized FSMFEH attains a power density of 2.28 mW/cm^3 at an external magnetic field of 1 500 μT/50 Hz. Applying this performance optimization method to existing studies, the maximum power density is increased by more than 3.02 times compared to the original results with the same external magnetic field and dimensions.**

***Index Terms*—Effective permeability, free-standing magnetic field energy harvester (FSMFEH), mathematical model, optimization, power density, sensor.**

I. INTRODUCTION

IN RECENT years, a significant number of sensors have been integrated into the power IoT for state sensing [1], [2], [3]. However, power supply has become a primary factor limiting the deployment of sensors [4]. The traditional method of powering through wired connections is inflexible and not suitable for distributed sensor networks. Batteries, due to their limited capacity, need to be replaced regularly, leading to high maintenance difficulty and cost [5]. Achieving self-powering has become crucial in advancing the application of sensors.

Energy harvesting technologies, which convert various environmental energy sources such as solar [6], wind [7], vibration [8], radio frequency [9], thermoelectric [10], electric field [11], and magnetic field [12] into electrical energy, have emerged as promising techniques for enabling self-powered sensors. Solar and wind energy harvesters are weather-prone and difficult to use indoors. Vibration energy harvesters are only applicable in certain scenarios with abundant vibrational energy sources, such as transformer casings. Radio frequency and thermoelectric energy harvesters produce extremely low output power. Electric field induction plates are large, difficult to install and pose a risk of breakdown. Magnetic field energy is widely distributed in the power grid, and harvesting and converting it into electrical energy can effectively address the power supply challenges for sensors.

Current transformer-based magnetic field energy harvesters have been widely studied [13], [14], [15], [16], [17]. These harvesters exhibit high power density, but they must be clamped to power lines and cannot power sensors on the low-voltage side [18]. Recently, researchers have begun to focus on the design of the free-standing magnetic field energy harvester (FSMFEH) [19], [20], [21]. With the nonclosed core, the FSMFEH can be flexibly installed in locations with ac magnetic fields in the power grid. Compared with cantilever-based magnetic field energy harvesters, the FSMFEH exhibits advantages in terms of long-term reliability, resistance to environmental interference, and operating frequency range. However, due to demagnetization reducing the effective permeability, the power density of the FSMFEH is relatively low [22]. Thus, the research focus on the FSMFEH lies in enhancing its power density.

The FSMFEH mainly consists of two components: the core and the coil. Typically, Mn-Zn ferrite is selected as the core material [19], [22], [23]. The high relative permeability of Mn-Zn ferrite is sufficient to saturate the effective permeability of the core, and its high resistivity allows for negligible eddy current

Received 26 November 2024; revised 28 February 2025; accepted 19 April 2025. Date of publication 25 April 2025; date of current version 30 June 2025. This work was supported in part by the Technology Program of China Southern Power Grid Company Ltd. under Program GDKJXM20222209(036100KK52222045) and in part by the National Natural Science Foundation of China under Program U2166214. Recommended for publication by Associate Editor S. A. Khajehoddin. *(Corresponding author: Aijun Yang.)*

Zhu Liu, Likai Zheng, Siyu Bao, Aijun Yang, Jifeng Chu, Huan Yuan, Mingzhe Rong, and Xiaohua Wang are with the State Key Laboratory of Electrical Insulation and Power Equipment, Xi'an Jiaotong University, Xi'an 710049, China (e-mail: xajtdxlz@stu.xjtu.edu.cn; zhenglikai@stu.xjtu.edu.cn; nini 1227@stu.xjtu.edu.cn; yangaijun@mail.xjtu.edu.cn; jfchu93@xjtu.edu.cn; huanyuan@xjtu.edu.cn; mzrong@mail.xjtu.edu.cn; xhw@mail.xjtu.edu.cn).

Dan Zhou is with the Guangdong Provincial Key Laboratory of Electric Power Equipment Reliability, Electric Power Research Institute of Guangdong Power Grid Company, Ltd., Guangzhou 510080, China (e-mail: zhoudan@gddky.csg.cn).

Color versions of one or more figures in this article are available at https://doi.org/10.1109/TPEL.2025.3564377.

Digital Object Identifier 10.1109/TPEL.2025.3564377

losses in the core. For the core shape, slender cores with a low demagnetization factor can enhance the effective permeability and power density [24]. However, in many scenarios where sensors need to be installed, spatial constraints can hinder the use of slender cores. Several special core shapes have been designed to increase the effective permeability with a limited core length, including dumbbell-shaped [23], bow-tie-shaped [25], H-shaped [26], and funnel-shaped [27], [28]. These cores exhibit structural similarities, with flux collectors at both ends and a thin rod in the middle, and can be approximated as the same category. The effectiveness of these cores in enhancing power density has been verified experimentally. Nonetheless, previous works have primarily relied on experiments and finite element simulations to optimize core parameters, which is time-consuming, costly, and difficult to obtain the optimal core structure. More importantly, it is challenging to derive generalized design guidelines for different core dimensions. In addition, the effect of coil parameters on the performance of the FSMFEH has not been comprehensively investigated. In fact, the correlation between core and coil parameters makes designing the FSMFEH through experiments and simulations even more difficult and complex.

Yang et al. [26] developed a mathematical model for the power density of the FSMFEH to derive generalized design guidelines. This model allows for the optimization of core and coil parameters. Since only ellipsoidal cores permit accurate calculation of the effective permeability, this model estimates the effective permeability of the H-shaped core using an equivalent structure. However, due to significant differences in the magnetic field distribution between the actual H-shaped core and the proposed equivalent structure, the accuracy of the calculated effective permeability by this model is relatively low. To improve the accuracy of the effective permeability calculation, a correction term in relation to the flux collector radius and thickness is introduced in [29]. Nevertheless, the corrected effective permeability still deviates considerably from the actual value when the rod radius is small. Moreover, Yang et al. [26] and Liu et al. [29] overlooked the differences in maximum power and maximum power density of the FSMFEH in determining the optimal core and coil parameters.

To address these issues, this work presents a modeling and optimization method for the FSMFEH that is predicated on the accurate estimation of effective permeability. Based on the effective permeability of cylindrical cores and flux continuity theorem, along with a correction term, an accurate estimation for the effective permeability of H-shaped cores is obtained. Subsequently, a mathematical model is established to describe the output characteristics of the FSMFEH. Using this model, the core and coil parameters are optimized to enhance the performance of the FSMFEH, and a performance optimization procedure is summarized. Specifically, the mutual interactions between the FSMFEH and power management circuit, as well as the differences in maximum power and maximum power density are analyzed in the optimization process. In addition, this work discusses the impact of coil current on core losses and how to fairly compare the performance of FSMFEHs with different external magnetic fields and dimensions.

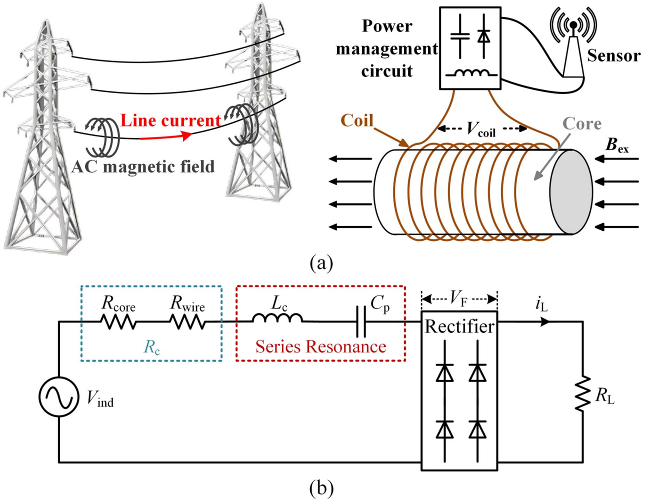

Fig. 1. (a) Schematic diagram. (b) Equivalent circuit of the FSMFEH.

The rest of this article is structured as follows. Section II introduces the method for estimating the effective permeability of H-shaped cores and establishes the mathematical model of the FSMFEH. In Section III, the performance optimization of the FSMFEH based on this model is discussed. In Section IV, the accuracy of the effective permeability estimation and the proposed model of the FSMFEH, as well as the effectiveness of the performance optimization method, are verified through experiments. Finally, Section V concludes this article.

II. MATHEMATICAL MODELING

A. Working Principle and Equivalent Circuit of the FSMFEH

The schematic diagram of the FSMFEH is illustrated in Fig. 1(a). The ac magnetic field around the electrical equipment is harvested by the core and generates an induced voltage in the coil based on electromagnetic induction. The ac voltage V_{coil} from the coil is converted by a power management circuit to power the sensor.

Fig. 1(b) shows the equivalent circuit of the FSMFEH. The induced voltage V_{ind} can be expressed as

$$V_{\text{ind}} = \omega \mu_e N A_c B_{\text{ex}} \tag{1}$$

where ω is the angular frequency of the magnetic field, μ_e is the effective permeability of the core, N is the number of coil turns, A_c is the cross-section area of the core, and B_{ex} is the external magnetic flux density.

The coil resistance R_c comprises the wire resistance R_{wire} and the core loss resistance R_{core}. Core losses mainly consist of hysteresis losses and eddy current losses. Hysteresis losses are considered negligible at low frequencies of 50/60 Hz. Eddy current losses inside the core are extremely low due to the high resistivity of Mn-Zn ferrite [25]. Therefore, R_c can be approximated as being equal to R_{wire}.

The compensating capacitor C_p is utilized to form a series resonance with the coil inductance L_c to improve the power

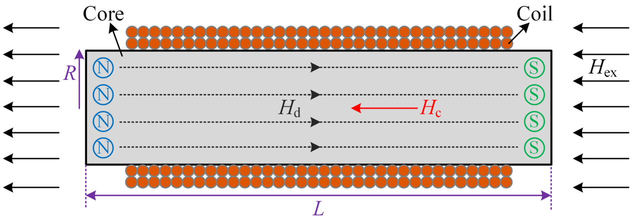

Fig. 2. Demagnetizing field H_d inside a nonclosed core.

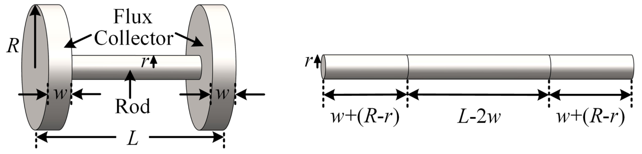

(a) (b)

Fig. 3. (a) H-shaped core. (b) Equivalent structure in [26].

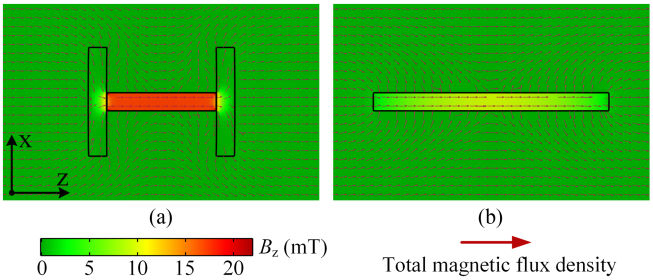

(a) (b)

Fig. 4. Simulated magnetic flux density of (a) The H-shaped core. (b) Equivalent structure.

transfer efficiency

$$L_c = \mu_0 \mu_e \frac{N^2 A_c}{l_{\text{core}}}, \quad C_p = \frac{1}{\omega^2 L_c} \tag{2}$$

where μ_0 and l_{core} represent the vacuum permeability and the length of the core covered by the coil, respectively. The load power P_L can be calculated as

$$P_L = i_L^2 \cdot R_L = \left(\frac{V_{\text{ind}} - V_F}{R_c + R_L}\right)^2 \cdot R_L \tag{3}$$

where V_F denotes the forward voltage drop of the rectifier, i_L and R_L are the load current and load resistance, respectively. The maximum load power can be obtained under impedance matching, i.e., $R_L = R_c$

$$P_L = (V_{\text{ind}} - V_F)^2 / 4R_c. \tag{4}$$

B. Estimation of Effective Permeability for H-Shaped Cores

The calculation of effective permeability is a crucial step in modeling the FSMFEH. As illustrated in Fig. 2, when the core is magnetized by an external magnetic field H_{ex}, the induced magnetic poles at its ends generate a demagnetizing field H_d opposite in direction to H_{ex}. As a result, the magnetic field H_c inside the core is lower than H_{ex} [24].

Due to the demagnetizing field, the effective permeability μ_e of a nonclosed core is usually much lower than the relative permeability μ_r of the core material. To enhance the effective permeability, the demagnetization factor D_M must be reduced. Slender cores should be used since D_M is directly proportional to *R*/*L* [24], where *R* and *L* are the core radius and core length, respectively. However, slender cores made of Mn-Zn ferrite are fragile. In addition, spatial constraints pose challenges for the installation of slender cores in practical scenarios. Due to their substantial spatial requirements, slender cores may also interfere with the normal operation of other equipment. As a result, FSMFEHs with slender cores face a design challenge in balancing installation flexibility and power density. In order to address this issue, the H-shaped core as illustrated in Fig. 3(a) has been designed, consisting of flux collectors at both ends and a thin rod in the middle. *L*, *R*, *w*, and *r* represent the core length, core radius, flux collector thickness, and rod radius of the H-shaped core, respectively. Compared with slender cores, the H-shaped core can achieve a higher effective permeability with a shorter core length, which promotes greater flexibility in installation. Moreover, the H-shaped core demonstrates a greater ability to gather the external magnetic field. The coil is wound around the thin rod of the H-shaped core, which can reduce the total length of the coil wire and the coil resistance, thereby enhancing the load power of the FSMFEH.

However, only the effective permeability of the cylindrical core can be directly estimated [26]. To estimate the effective permeability of the H-shaped core, an equivalent structure as depicted in Fig. 3(b) is proposed in [26], with a radius *r* and a length L_{eq} equal to *L*+2*R*-2*r*. The effective permeability of this equivalent structure is given by

$$\mu_{e,\text{eq}} = \frac{\mu_r}{1 + \frac{1.7 a_{\text{eq}}^{0.13}}{b_{\text{eq}}^3} \left(\frac{1}{2a_{\text{eq}}}\right)^2 \left[\ln\left(\frac{1+b_{\text{eq}}}{1-b_{\text{eq}}}\right) - 2b_{\text{eq}}\right] (\mu_r - 1)} \tag{5}$$

where $a_{\text{eq}} = L_{\text{eq}}/2r$, $b_{\text{eq}} = (1\text{-}1/a_{\text{eq}}{}^2)^{1/2}$. Although the equivalent structure reflects the flux path length of the H-shaped core, its ability to gather the magnetic field is weaker than that of the H-shaped core with flux collectors. Therefore, compared with the actual H-shaped core, the effective permeability calculated using the equivalent structure is underestimated, which can be validated by the finite element simulation of the magnetic flux density shown in Fig. 4.

The simulation model is built using the "Magnetic Fields" interface in COMSOL software. Frequency-domain analysis at 50 Hz is employed for all studies. The core is placed in an air domain surrounded by an infinite element domain (not shown in the figure). The "Reduced Field" in the "Magnetic Fields" interface is used to generate a spatially uniform magnetic field along the *Z*-axis, with a flux density set to 100 μT. The *L*, *R*, *w*, and *r* of the H-shaped core are 8, 3, 1, and 0.5 cm, respectively. The core material is selected as PC95 Mn-Zn ferrite. It is observed that the flux density (9.37 mT) across the middle cross-section of the equivalent structure is significantly lower than that (17.31 mT) of the actual H-shaped core.

Another major issue with the equivalent structure is that its length, *L*+2*R*-2*r*, is independent of the collector thickness *w*,

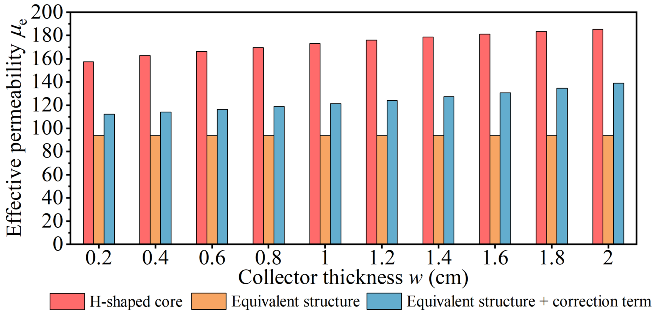

Fig. 5. Simulated effective permeability of the H-shaped core and the equivalent structure with/without the correction term for different collector thicknesses.

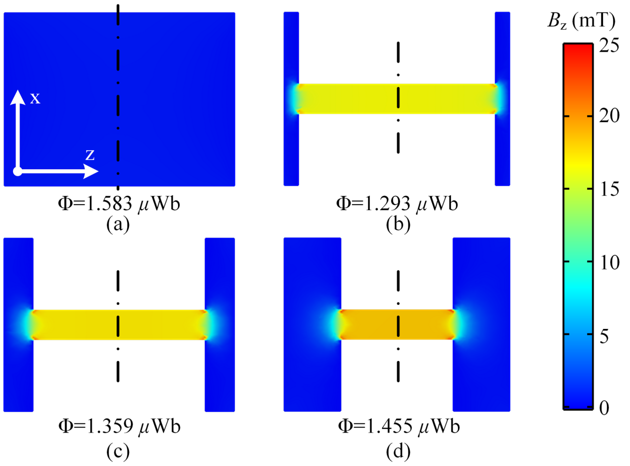

Φ=1.583 μWb
(a)

Φ=1.293 μWb
(b)

Φ=1.359 μWb
(c)

Φ=1.455 μWb
(d)

Fig. 6. Total magnetic flux and flux density inside the cores. (a) Cylindrical. (b) H-shaped, $w = 0.5$ cm, $r = 0.5$ cm. (c) H-shaped, $w = 1$ cm, $r = 0.5$ cm. (d) H-shaped, $w = 2$ cm, $r = 0.5$ cm. (In all cases, $L = 8$ cm, $R = 3$ cm).

thus failing to reflect the impact of the collector thickness on effective permeability of the H-shaped core. To address this issue, a correction term $[(L+2R-2r)/(L-2w)]^{1/3}$, which is related to the core radius and collector thickness, is further introduced in [29]. Consequently, the effective permeability of equivalent structure can be rewritten as

$$\mu_{e,\mathrm{eq}} = \frac{\left[(L+2R-2r)\,/\,(L-2w)\right]^{1/3}\cdot\mu_r}{1+\frac{1.7a_{\mathrm{eq}}^{0.13}}{b_{\mathrm{eq}}^{3}}\left(\frac{1}{2a_{\mathrm{eq}}}\right)^{2}\left[\ln\left(\frac{1+b_{\mathrm{eq}}}{1-b_{\mathrm{eq}}}\right)-2b_{\mathrm{eq}}\right](\mu_r-1)}. \tag{6}$$

Fig. 5 displays the simulated effective permeability of the H-shaped core and the equivalent structure with/without the correction term for different collector thicknesses. It can be seen that the correction term reflects the trend of the effective permeability with changing collector thickness. However, due to the inherently low effective permeability of the equivalent structure, the results with the correction term still significantly differ from those of the actual H-shaped core, with a minimum error of up to 25.06%.

Essentially, the effective permeability $\mu_{e,H}$ of the H-shaped core is the ratio of the flux density B_{rod} within the rod to the external flux density B_{ex}. To accurately estimate the effective permeability of the H-shaped core, a novel method is proposed based on the effective permeability of the cylindrical core and flux continuity theorem, along with a correction term.

Step 1: For the H-shaped core, it can be conceptualized as an adaptation of the cylindrical core with a reduced cross-section area at its midsection. If the magnetic flux entering the core remains constant before and after the reduction of the midsection's cross-section area, the flux density in the flux collector of the H-shaped core, denoted as B_{collect}, should equal the flux density in the cylindrical core, denoted as B_{cylinder}. However, the reduction of the midsection's cross-section area of the cylindrical core will result in an increased magnetic reluctance along the direction of the external magnetic field, leading to a decrease in the magnetic flux entering the core, as shown in Fig. 6. Compared to the cylindrical core, a smaller flux collector thickness w, or a smaller rod radius r results in less magnetic flux entering the H-shaped core, thus decreasing the ratio of B_{collect} to B_{cylinder}. In order to quantify the difference in magnetic flux between the two types of cores, a correction term related to both w and r is introduced

$$\frac{B_{\mathrm{collect}}}{B_{\mathrm{cylinder}}} = k\left(\frac{w}{L}, \frac{r}{R}\right). \tag{7}$$

Step 2: In order to derive the correction term, finite element simulations are conducted to obtain the flux densities, B_{cylinder} in the cylindrical core and B_{collect} in the flux collector of the H-shaped cores with varying w/L and r/R ratios, under the same external flux density B_{ex}. These simulated datasets of flux densities are substituted into (7) to determine the specific values of the correction term $k(w/L, r/R)$ under different w/L and r/R conditions. Then, a fitting process is conducted, taking the numerical values of w/L and r/R as independent variables and the corresponding values of $k(w/L, r/R)$ as the dependent variable, thereby yielding a specific functional form of $k(w/L, r/R)$ in terms of w/L and r/R. Taking into account the accuracy, simplicity, and universality of the function, the expression for the fitted $k(w/L, r/R)$ is presented as

$$k\left(\frac{w}{L}, \frac{r}{R}\right) = \left[0.445\left(\frac{w}{L}\right)^{0.55}+0.9\right] \times \left[0.249\left(\frac{r}{R}\right)^{1.14}+0.736\right]. \tag{8}$$

Step 3: The relative permeability of core materials is much higher than that of air. For the H-shaped core, according to the flux continuity theorem, the total magnetic flux ϕ_{collect} through the cross-section of the flux collector is essentially equal to the total magnetic flux ϕ_{rod} through the cross-section of the rod. Since the magnetic flux is the product of cross-sectional area and flux density, the ratio of the flux density B_{collect} in the flux collector to the flux density B_{rod} in the rod satisfies

$$\frac{B_{\mathrm{collect}}}{B_{\mathrm{rod}}} = \frac{r^2}{R^2}. \tag{9}$$

Step 4: The effective permeability $\mu_{e,H}$ of the H-shaped core can be derived through a series of mathematical operations.

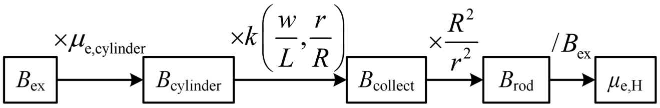

Fig. 7. Estimation process for the effective permeability $\mu_{e,H}$ of the H-shaped core.

Substituting (7) into (9) yields

$$B_{\text{rod}} = B_{\text{cylinder}} \cdot \frac{R^2}{r^2} \cdot k\left(\frac{w}{L}, \frac{r}{R}\right). \tag{10}$$

Dividing both sides of (10) by the external flux density B_{ex}, the expression for $\mu_{e,H}$ can be represented as

$$\mu_{e,H} = \frac{B_{\text{rod}}}{B_{\text{ex}}} = \frac{B_{\text{cylinder}}}{B_{\text{ex}}} \cdot \frac{R^2}{r^2} \cdot k\left(\frac{w}{L}, \frac{r}{R}\right) = \mu_{e,\text{cylinder}} \cdot \frac{R^2}{r^2} \cdot k\left(\frac{w}{L}, \frac{r}{R}\right). \tag{11}$$

Thus, $\mu_{e,H}$ can be derived from (8), (11), and the effective permeability of the cylindrical core presented in [26] and [29]

$$\mu_{e,H} = \frac{\mu_r \left[0.445\left(\frac{w}{L}\right)^{0.55} + 0.9\right] \left[0.249\left(\frac{r}{R}\right)^{1.14} + 0.736\right]}{1 + \frac{1.7a^{0.13}}{b^3}\left(\frac{1}{2a}\right)^2 \left[\ln\left(\frac{1+b}{1-b}\right) - 2b\right](\mu_r - 1)} \cdot \frac{R^2}{r^2} \tag{12}$$

where $a = L/2R$, $b = (1\text{-}1/a^2)^{1/2}$. Based on the above-mentioned analysis, the estimation process for the effective permeability $\mu_{e,H}$ of the H-shaped core is summarized in Fig. 7.

For different overall dimensions of the H-shaped core, i.e., different combinations of core length L and core radius R, the functional form of the correction term $k(w/L, r/R)$ exhibits a high degree of consistency. This is attributed to the fact that the variables in $k(w/L, r/R)$ are the ratio of the flux collector thickness w to the core length L, and the ratio of the rod radius r to the core radius R, both of which are dimensionless, thus eliminating the impact of the absolute values of L and R. For different combinations of L and R, the effective permeability of H-shaped cores with various w/L and r/R ratios is estimated by (12). Meanwhile, the actual effective permeability of these H-shaped cores is determined through finite element analysis. The relative errors between the estimation and simulation results are depicted in Fig. 8. It can be observed that for H-shaped cores with different combinations of L and R, the relative errors between the estimated and simulated effective permeability consistently remain below 9% across various w/L and r/R conditions. This demonstrates the high accuracy and universality of the proposed correction term and effective permeability estimation method.

C. Mathematical Model of the FSMFEH

Fig. 9(a) shows the cross-section of the FSMFEH, where h is the coil height. To maximize the power density, the coil turns are densely arranged as illustrated in Fig. 9(b). r_w and δ are the wire radius and insulation thickness, respectively. The number of coil turns N can be derived as

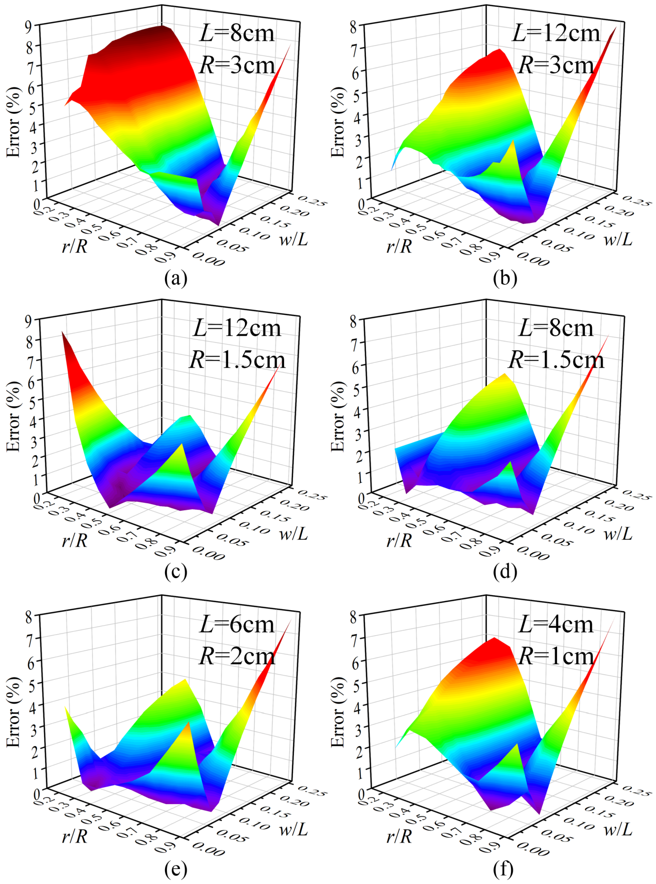

Fig. 8. Relative errors between the estimation and simulation results of effective permeability $\mu_{e,H}$ for different combinations of L, R, w, and r. (a) $L =$ 8 cm, $R =$ 3 cm, (b) $L =$ 12 cm, $R =$ 3 cm, (c) $L =$ 12 cm, $R =$ 1.5 cm, (d) $L =$ 8 cm, $R =$ 1.5 cm, (e) $L =$ 6 cm, $R =$ 2 cm, (f) $L =$ 4 cm, $R =$ 1 cm.

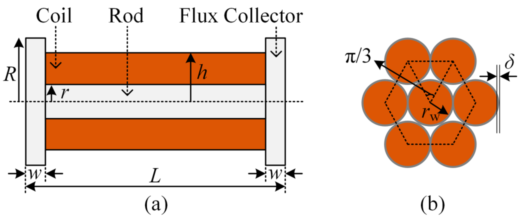

Fig. 9. (a) Cross-section of the FSMFEH. (b) Densely arranged coil turns.

$$N = \frac{\eta S_c}{S_{\text{wire}}} = \frac{\sqrt{3}\,(L - 2w)\,(h - r)}{6(r_w + \delta)^2} \tag{13}$$

where S_c and η are the cross-section area and filling factor of the coil, respectively, and S_{wire} is the cross-section area of the enameled wire. The induced voltage V_{ind} can be expressed as

$$V_{\text{ind}} = \frac{\sqrt{3}\pi\omega\mu_{e,H} B_{\text{ex}}\,(L - 2w)\,(h - r)\, r^2}{6(r_w + \delta)^2} \tag{14}$$

where $\mu_{e,H}$ is determined by (12). The coil resistance R_c can be calculated as

$$R_c = \rho \frac{N \cdot l_{\text{turn}}}{\pi r_w^2} = \frac{\sqrt{3}\rho\,(L-2w)\left(h^2-r^2\right)}{6(r_w+\delta)^2 r_w^2} \tag{15}$$

where ρ and l_{turn} are the wire resistivity and average length of a single coil turn. Then, the load power P_L can be calculated from (4), (12), (14), and (15). According to the volume V_{ol} of the FSMFEH, which includes both the core and coil volumes, the power density D_p can be calculated as

$$D_p = \frac{P_L}{V_{\text{ol}}} = \frac{P_L}{2w\pi R^2 + \pi h^2 (L-2w)}. \tag{16}$$

In the next section, based on the established mathematical model, the core and coil parameters will be optimized to enhance the performance of the FSMFEH.

III. PERFORMANCE OPTIMIZATION

Due to the typically limited installation space in practical applications, the optimization for the FSMFEH in this work is conducted within a fixed space. The core length L and core radius R are fixed at 80 mm and 20 mm, respectively, as an example. PC95 Mn-Zn ferrite with a relative permeability μ_r of 3300 is selected as the core material. The external magnetic field is established at 500 μT with a frequency of 50 Hz. The load resistance R_L is always set equal to the coil resistance R_c for impedance matching.

A. Coil Height Selection

To simplify the analysis, the forward voltage drop V_F of the rectifier is initially set to 0. The wire radius r_w is chosen to be 0.15 mm, with an insulation thickness δ of 0.019 mm. When the wire radius is constant, optimizing the coil height also reflects the optimization of the number of coil turns N.

Fig. 10 shows the correlation between the load power P_L, power density D_p and coil height h for various core geometric parameters. It can be observed that P_L consistently increases with h. However, there may be an optimal value of h (denoted as h_{opt}) which maximizes D_p. These results can be analyzed through the mathematical model in Section II. When V_F is 0, P_L can be simplified according to (4), (14), and (15) as

$$P_L = \frac{\sqrt{3}\pi^2\omega^2\mu_{e,H}^2 B_{\text{ex}}^2 (L-2w)\, r^4 r_w^2}{24\rho (r_w+\delta)^2} \cdot \frac{h-r}{h+r}. \tag{17}$$

Taking the derivative of P_L with respect to h yields

$$\frac{dP_L}{dh} = \frac{\sqrt{3}\pi^2\omega^2\mu_{e,H}^2 B_{\text{ex}}^2 (L-2w)\, r^4 r_w^2}{12\rho (r_w+\delta)^2} \cdot \frac{r}{(h+r)^2} > 0. \tag{18}$$

Since dP_L/dh is always greater than zero, P_L monotonically increases with h. Substituting (17) into (16) yields

$$D_p = \frac{\sqrt{3}\pi^2\omega^2\mu_{e,H}^2 B_{\text{ex}}^2 (L-2w)\, r^4 r_w^2 \,(h-r)}{24\rho (r_w+\delta)^2 (h+r)\left[2w\pi R^2 + \pi h^2 (L-2w)\right]}. \tag{19}$$

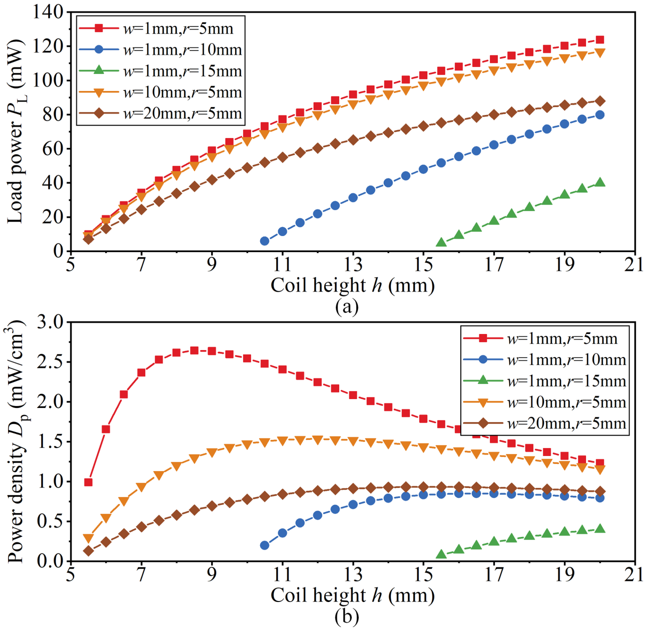

(a)

(b)

Fig. 10. (a) Load power. (b) Power density against the coil height h for various core geometric parameters ($r < h \leq R$).

Taking the derivative of D_p with respect to h and setting dD_p/dh to zero, the simplification yields

$$h_{\text{opt}}^3 - r h_{\text{opt}}^2 - r^2 h_{\text{opt}} - \frac{2wrR^2}{L-2w} = 0, \quad h_{\text{opt}} > r. \tag{20}$$

When $r < h < h_{\text{opt}}$, D_p increases with h. When $h > h_{\text{opt}}$, D_p decreases with the increase of h. According to (20), h_{opt} is determined by the core geometric parameters. Actually, the primary objective in optimizing the FSMFEH is to maximize power density rather than simply maximizing load power. This is due to the fact that the increase in load power comes at the cost of larger volume and weight, whereas power density more accurately reflects the performance level of the FSMFEH. Only when the power produced by the FSMFEH at maximum power density conditions is insufficient to meet the load power requirement, is it necessary to increase the coil height h to enhance power until the load power requirement is satisfied.

B. Optimization of Core Geometric Parameters

Fig. 11 presents the load power P_L and power density D_p under different collector thicknesses w and rod radii r. The maximum load power P_L, which occurs when h is equal to R, initially increases slightly with w before decreasing, with the maximum value obtained at $w = 3$ mm. When w is less than 5 mm, the relative differences in maximum P_L for different w are less than 2%. However, the maximum power density D_p, which occurs when h is equal to h_{opt}, decreases significantly with w. Considering both the maximum P_L and maximum D_p, the collector thickness w should be minimized.

Both the maximum P_L and the maximum D_p decrease with the increase of the rod radius r, which is consistent with the simulation results in [25]. Thus, a smaller rod radius r should be selected. Although smaller values of collector thickness w

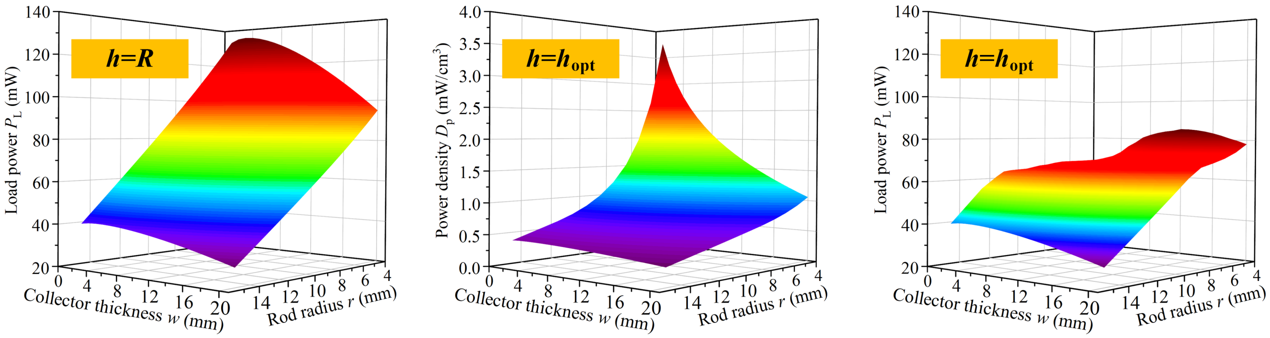

(a) (b) (c)

Fig. 11. (a) Maximum P_L, $h = R$. (b) Maximum D_p, $h = h_{\text{opt}}$. (c) P_L at the maximum D_p, $h = h_{\text{opt}}$ for different combinations of w and r.

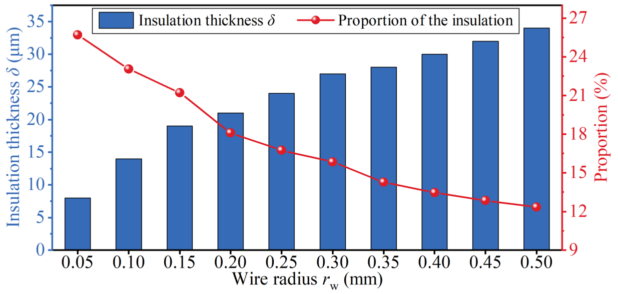

Fig. 12. Insulation thickness δ and the proportion of the insulation to the total cross-section area of the enameled wire for different wire radii r_w.

and rod radius r are beneficial for enhancing the power density of the FSMFEH, it is imperative to concurrently consider the mechanical strength and manufacturing complexity of the H-shaped core.

The load power P_L at maximum power density condition is shown in Fig. 11(c). Compared to the maximum P_L shown in Fig. 11(a), the P_L at the maximum D_p is significantly lower, especially when w and r are small. Therefore, if the P_L at the maximum D_p is lower than the load power requirement, the coil height should be increased.

C. Wire Radius Selection

In this part, the collector thickness w, rod radius r, and coil height h are selected as 2, 4, and 20 mm, respectively. When the coil height is constant, optimizing the wire radius also reflects the optimization of the number of coil turns N.

According to (17), the load power P_L is independent of wire radius r_w under impedance matching conditions, disregarding the forward voltage drop V_F of the rectifier and insulation thickness δ. Nevertheless, the manufacturer's data indicates that the insulation thickness δ increases with r_w, while the proportion of the insulation to the total cross-section area of the enameled wire decreases, as shown in Fig. 12. Therefore, a larger r_w means less space wasted by the insulation and a higher load power P_L. As illustrated in Fig. 13, if V_F is 0 V, increasing r_w from 0.05 to 0.5 mm will enhance P_L from 127.5 to 150.4 mW.

In practice, the forward voltage drop V_F of the rectifier is typically non-negligible. Since the minimum forward voltage drop of a single diode is about 0.2 V, the V_F is at least 0.4 V. According to (1), (4), and (13), the increase in wire radius r_w reduces the number of coil turns N and induced voltage V_{ind}, which increases the loss caused by V_F and may diminish the power delivered to the load. Fig. 13 shows that as r_w increases from 0.05 to 0.5 mm, V_{ind} decreases from 94.72 to 1.12 V. The P_L initially increases and then decreases, with a maximum value of 127.7 mW achieved at $r_w = 0.1$ mm. In addition, the selected r_w should ensure that V_{ind} falls within the operating voltage range of the elements in the power management circuit. Excessively low or high V_{ind} may cause the circuit elements to fail to start properly or be damaged. Fluctuations in external magnetic fields are common in practical application scenarios. To ensure a stable power supply to the load over a wide range of external magnetic fields, r_w should be primarily selected based on weak magnetic field conditions. This is because the power output capability of the FSMFEH is relatively low under weak external magnetic fields, and balancing both the power density and the induced voltage is crucial at this point. As the external magnetic field intensifies, even if the selected r_w is not the optimal value for this magnetic field condition, the power density can still be maintained at a high level to meet the load power requirements. If the induced voltage is too high and may damage the circuit, protective measures such as voltage regulation and energy dissipation can be employed.

For performance optimization of the FSMFEH, parameters such as L, R, w, r, h, and r_w are interrelated and cannot be

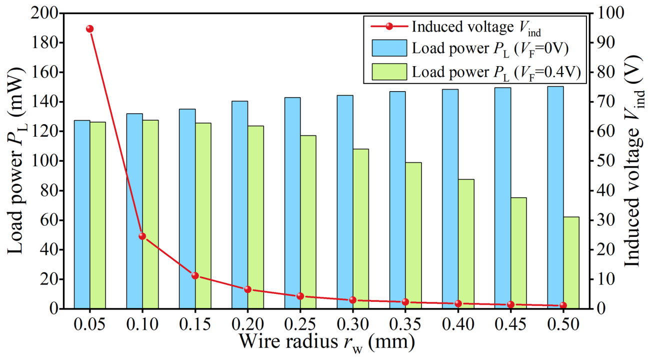

Fig. 13. Load power P_L and induced voltage V_{ind} for different wire radii r_w.

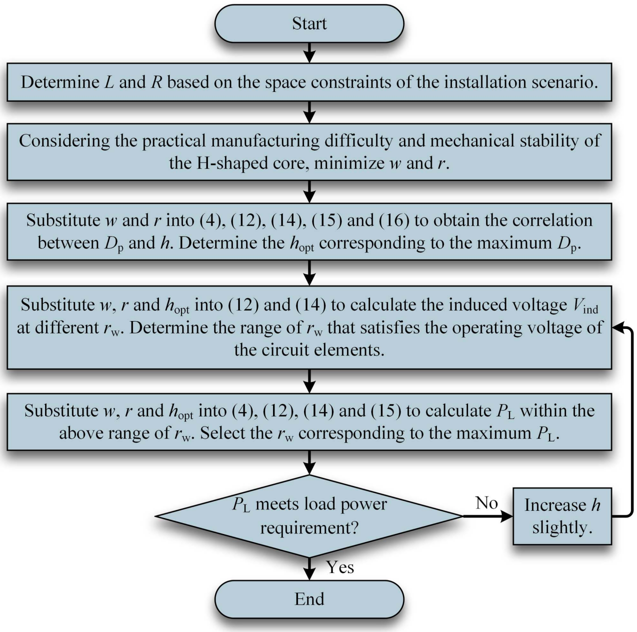

Fig. 14. Performance optimization procedure for the FSMFEH.

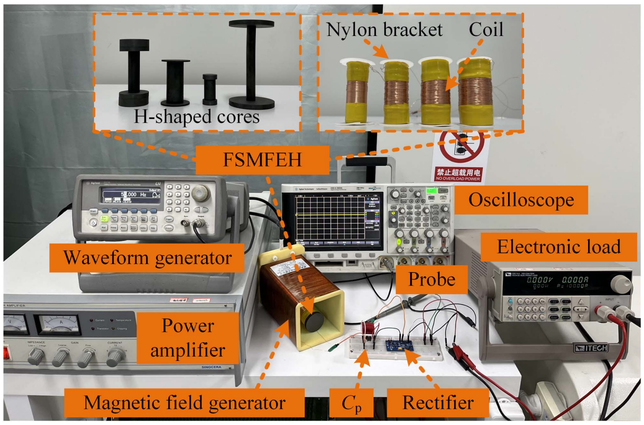

Fig. 15. Photograph of the experimental platform.

analyzed independently. Thus, it is necessary to determine the optimal core and coil parameters based on the mathematical model proposed in this work. According to the above-mentioned analysis of the core and coil parameters, a performance optimization procedure for the FSMFEH is summarized as shown in Fig. 14.

IV. EXPERIMENTAL VERIFICATION

A. *Experimental Setup*

In order to verify the accuracy of the effective permeability estimation and the developed mathematical model, as well as the effectiveness of the performance optimization method, an experimental platform, as shown in Fig. 15, is constructed.

The waveform generator and power amplifier supply the current to the winding of the magnetic field generator, which is designed to produce an external magnetic field applied to the FSMFEH. The flux collectors and rods are fabricated with PC95 Mn-Zn ferrite material to form H-shaped cores with various geometric parameters. The coil is wound around a 3-D-printed nylon bracket and combined with the H-shaped core to form the FSMFEH. The compensating capacitor C_p, rectifier, and electronic load are connected to the FSMFEH according to the circuit shown in Fig. 1(b). The oscilloscope and probe are utilized for measuring the load voltage waveform. In the experiments, the external magnetic field is set to 500 μT/50 Hz.

B. *Estimation of Effective Permeability*

To obtain the effective permeability $\mu_{e,H}$ of the H-shaped core, the coil is disconnected from the circuit and the induced voltage V_{ind} is measured. Subsequently, $\mu_{e,H}$ can be derived by solving (1). Fig. 16 compares the experimental and estimated results of effective permeability $\mu_{e,H}$ of the H-shaped cores with various combinations of L, R, r, and w. For H-shaped cores with various geometric parameters, the errors in the effective permeabilities obtained in [26] and [29] relative to the experimental results are 11.9%–45.2% and 2.4%–36.5%, respectively. In contrast, the errors in this work are only 1.9%–7.2%.

The estimation errors primarily stem from two sources. First, the correction term $k(w/L, r/R)$ is obtained by fitting the actual magnetic flux data, with the fitting process designed to minimize the error function. However, due to the limitations of the fitting function, the fitted correction term inevitably exhibits some deviation from the actual data. According to (11), this deviation will lead to a certain degree of inaccuracy in the estimation of effective permeability. Second, the expression for the effective permeability of cylindrical cores is an approximation derived from that of the ellipsoidal core, thus inherently containing some errors. The errors arising from these two sources are inherent and difficult to eliminate completely. However, the error range of the estimation method proposed in this work is significantly lower than those reported in [26] and [29]. Given that the geometric parameters of these H-shaped cores in Fig. 16 encompass a wide range of L, R, r, and w, the high accuracy and universality of the proposed effective permeability estimation method are validated by these representative data.

C. *Performance Optimization*

Considering the spatial constraints of the application scenarios, subsequent optimizations for the FSMFEH are carried out with the core length L and core radius R fixed at 80 mm and 20 mm, respectively, as an example. As mentioned in Section III-A, the primary objective of optimizing the FSMFEH is to enhance the power density. Fig. 17 illustrates the correlation between the load power P_L, power density D_p, and coil height h for different collector thicknesses w. The P_L consistently increases with h, but there exists a maximum value for D_p. For different w, the relative differences in maximum P_L are below 1.7% when w is less than 6 mm, but the maximum D_p drops significantly with increasing w. Therefore, the collector thickness w should be minimized. It is also noted that, as shown in Fig. 16, the experimental effective permeability $\mu_{e,H}$ is slightly higher than the estimated results. However, the experimental

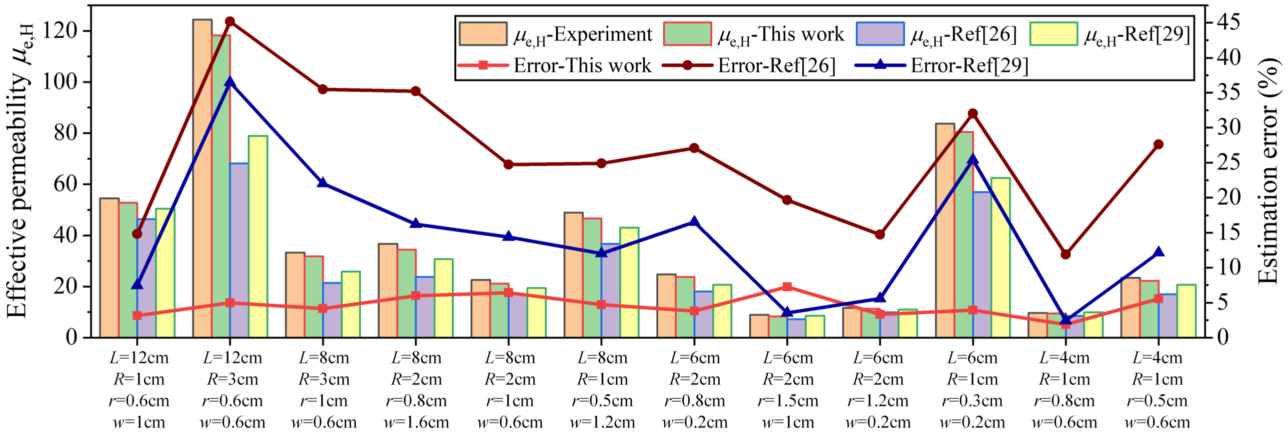

Fig. 16. Experimental and estimated $\mu_{e,H}$ under different core geometric parameters, along with the estimation errors.

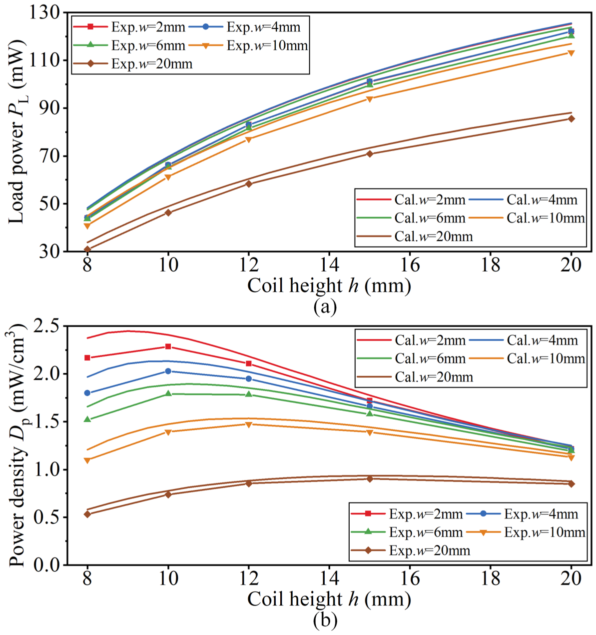

Fig. 17. (a) Load power. (b) Power density versus coil height for different collector thickness w ($r = 5$ mm, $r_w = 0.15$ mm).

power density D_p is slightly lower than the estimated results. This can be attributed to three main reasons. First, the thickness of the 3-D-printed nylon bracket is about 0.5 mm, resulting in a small portion of the coil space being wasted. Second, due to the inability to continuously adjust the capacitance in the experiment, the compensating capacitor C_p cannot fully resonate in series with the coil inductance L_c. Finally, in the experiment, the coil turns cannot be densely arranged exactly as shown in Fig. 9(b). Overall, the experimental results agree well with the calculations, which validates the accuracy of the established mathematical model for the FSMFEH.

Fig. 18 shows the maximum power density D_p for different rod radii r. It can be observed that the maximum D_p decreases with an increase in r, which is consistent with the theoretical analysis. Due to the brittleness of Mn-Zn ferrite, the mechanical

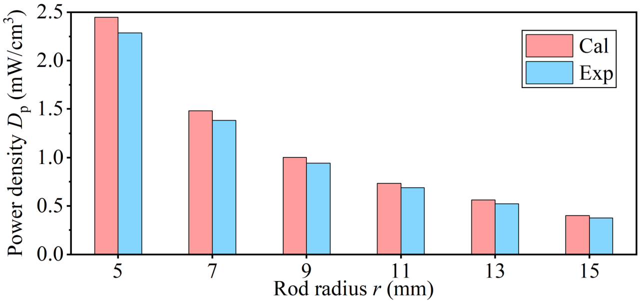

Fig. 18. Maximum power density D_p for different rod radii r ($w = 2$ mm, $h = h_{\text{opt}}$, $r_w = 0.15$ mm).

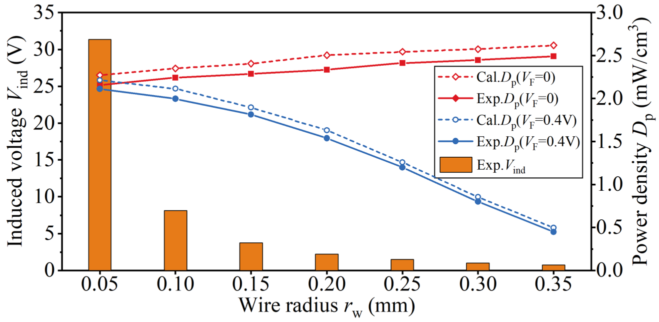

Fig. 19. Induced voltage V_{ind} and power density D_p for various wire radii r_w ($w = 2$ mm, $r = 5$ mm, $h = 10$ mm).

stability of the core should also be considered when selecting the rod radius r.

The induced voltage V_{ind} and power density D_p for different wire radii r_w are illustrated in Fig. 19. When the forward voltage drop V_F of the rectifier is equal to 0, the D_p increases with r_w. This is due to the fact that the increase in wire radius results in less space wasted by the insulation. In the experiment, the case where V_F is equal to 0 cannot be directly experimented upon using the circuit depicted in Fig. 1(b), since actual rectifiers inevitably exhibit a certain forward voltage drop. To address this issue, the rectifier is removed from the circuit, and the load resistance R_L is directly connected to the ac side. In this case, the

TABLE I
CORES CONSISTING OF DIFFERENT MATERIALS

Cores	Flux Collector Material	Rod Material
Core 1	PC95 Mn-Zn Ferrite	PC95 Mn-Zn Ferrite
Core 2	PC95 Mn-Zn Ferrite	1J85 Permalloy
Core 3	1J85 Permalloy	PC95 Mn-Zn Ferrite
Core 4	1J85 Permalloy	1J85 Permalloy

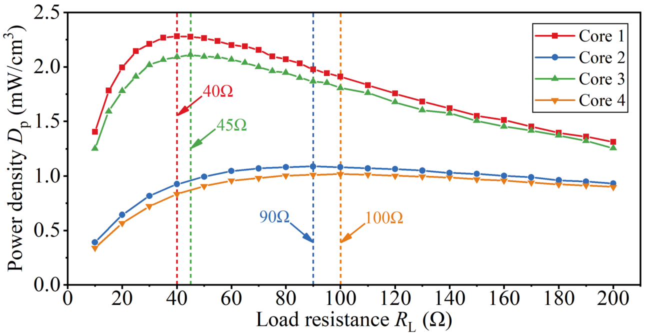

Fig. 20. Power density D_p versus load resistance R_L for the FSMFEHs with different cores ($w = 2$ mm, $r = 5$ mm, $h = 10$ mm, $r_w = 0.15$ mm).

D_p are calculated by measuring the rms value of the ac voltage across R_L. When the rectifier is connected in the circuit, the D_p drops from 2.11 to 0.45 mW/cm^3 as r_w increases from 0.05 to 0.35 mm. The diodes employed in the rectifier is SS52, with a forward voltage drop of about 0.2 V. If considering solely the enhancement of power density, r_w should be selected as 0.05 mm. However, it is also necessary to ensure that V_{ind} falls within the operating voltage range of the elements in the power management circuit.

To validate the advantages of Mn-Zn ferrite material over the 1J85 permalloy utilized in [26], four H-shaped cores made of different materials are fabricated, as illustrated in Table I. The power density D_p of the FSMFEHs with these cores is presented in Fig. 20. The maximum D_p (1.02 mW/cm^3) of the FSMFEH with core 4 is only 44.7% of that (2.28 mW/cm^3) with core 1. This is primarily due to the high conductivity of 1J85 permalloy (1.8×10^6 S/m), which causes severe eddy current losses in the core and increases the coil resistance R_c in the equivalent circuit shown in Fig. 1(b). According to (3) and (4), the R_L matched to R_c increases significantly, resulting in a decrease in maximum D_p.

From the above-mentioned analysis, it is evident that eddy current losses are an important consideration when selecting the core material for the FSMFEH. In [25], the eddy current losses induced by the external magnetic field under the open-circuit conditions are analyzed. However, when the load resistance R_L is connected, the magnetic field produced by the coil current i_c emerges as the decisive factor causing eddy current losses in the core. The coil current can be expressed as

$$i_c = \frac{V_{\text{ind}}}{R_c + R_L} = \frac{N\omega\mu_e A_c B_{\text{ex}}}{R_c + R_L}. \tag{21}$$

Therefore, the flux density B_s in the core induced by the coil current is given by

$$B_s = \frac{\mu_0\mu_e N i_c}{l_{\text{core}}} = \frac{\mu_0\mu_e^2 N^2\omega A_c B_{\text{ex}}}{l_{\text{core}}\,(R_c + R_L)}. \tag{22}$$

Substituting (2) into (22) yields

$$B_s = \frac{\mu_e B_{\text{ex}}\omega L_c}{R_c + R_L} = \frac{\omega L_c}{R_c + R_L}\cdot B_{\text{oc}} \tag{23}$$

where B_{oc} represents the flux density in the core induced by the external magnetic field. The coil inductance ωL_c of the FSMFEH is typically much higher than the coil resistance R_c, which is validated by the findings in [19], [23], [25], [26], and [27]. As a result, under impedance matching conditions, the flux density B_s in the core induced by the coil current satisfies

$$B_s = \frac{\omega L_c}{2R_c}\cdot B_{\text{oc}} \gg B_{\text{oc}}. \tag{24}$$

According to the Steinmetz equation [30], the core losses per unit volume can be expressed as

$$P_{\text{Fe}} = C_m \cdot f^{\alpha} \cdot B^{\beta} \tag{25}$$

where P_{Fe} is the core losses per unit volume, f is the frequency of the magnetic field, B is the magnetic flux density, and C_{m}, α, and β are the Steinmetz coefficients determined by the properties of the core material. Typically, α ranges from 1 to 2, while β ranges from 2 to 3. It can be concluded from (25) that the core losses per unit volume significantly increase with the magnetic flux density. Therefore, for the FSMFEH, the eddy current losses in the core are primarily caused by the flux density B_s induced by the coil current, rather than the flux density B_{oc} induced by the external magnetic field. This aspect has not been identified in previous studies [23], [25], [29]. Furthermore, it is observed that the D_p of the FSMFEHs with cores 2 and 4 are similar to each other, while those with cores 1 and 3 are also similar. This indicates that the eddy current losses in the permalloy core mainly occur in the rod rather than in the flux collectors. This is attributed to the much higher flux density in the rod compared to that in the flux collectors, as illustrated in Fig. 4. According to (25), it can be inferred that the core losses per unit volume in the rod is significantly greater than that in the flux collectors. In addition, the flux collector thickness should be minimized to maximize power density. Thus, the volume of the flux collectors does not significantly exceed that of the rod. Considering both volume and core losses per unit volume, it can be concluded that core losses mainly occur in the rod.

D. Comparison and Discussion

A comparison between the previous studies [21], [23], [25], [26], [29] and this work is summarized in Table II. Compared to the method of designing the FSMFEH through simulation in [21] and [25], the optimal core and coil parameters can be directly calculated using the mathematical model developed in this work, which greatly reduces the time and difficulty required to design the FSMFEH. Estimation of the effective permeability is the key to the mathematical modeling of the FSMFEH. As demonstrated in Fig. 16, compared to [26] and [29], this work further improves

TABLE II
COMPARISON BETWEEN THE PREVIOUS STUDIES AND THIS WORK

	[21]	[23]	[25]	[26]	[29]	This work
External magnetic field	About 600 μT/50 Hz	160 μT/50 Hz	7 μT/50 Hz	About 1 mT/50 Hz	200 μT/50 Hz	500 μT/50 Hz
Dimensions (cm × cm × cm)	5 × 3.8 × 3.8	17 × 5 × 5	15 × 10 × 10	4 × 3 × 3	6 × 4 × 4	8 × 4 × 4
Core shape	Cylinder-shaped	Dumbbell-shaped	Bow-tie-shaped	H-shaped	H-shaped	H-shaped
Core material	Mn-Zn ferrite	Steel and ferrite	Mn-Zn ferrite	Permalloy	Mn-Zn ferrite	Mn-Zn ferrite
Design method	Simulation and calculation	No optimization	Simulation and calculation	Calculation	Calculation	Calculation
Consider the operating voltage of the circuit	Yes	No	No	No	Yes	Yes
Load power P_{L}	4.38 mW	40.5 mW	360 μW	13.25 mW	6.33 mW	121.9 mW
Power density D_{p}	90.38 μW/cm^3	121.3 μW/cm^3	0.904 μW/cm^3	368 μW/cm^3	83.9 μW/cm^3	2.28 mW/cm^3
Optimized maximum P_{L} (without/with rectifier losses)	48.68/44.64 mW	217.3/198.5 mW	1.21/1.06 mW	42.35/39.27 mW	10.04/9.03 mW	129.6/121.9 mW
Optimized maximum D_{p} (without/with rectifier losses)	1.49/1.32 (mW/cm^3)	2.06/1.83 (mW/cm^3)	3.12/2.73 (μW/cm^3)	3.39/3.08 (mW/cm^3)	345/299 (μW /cm^3)	2.49/2.28 (mW/cm^3)

the model accuracy of the FSMFEH by accurately estimating the effective permeability. The mathematical model proposed in this work serves as a universal tool for designing and optimizing the FSMFEHs with various external magnetic fields and dimensions. By substituting the specific values of the external magnetic field and dimensions into the model, the maximum load power, power density, and corresponding design parameters can be obtained.

As can be seen from Table II, existing studies on the FSMFEH demonstrate significant differences in terms of external magnetic field and dimensions. Since the load power of the FSMFEH is directly affected by external magnetic fields and dimensions, it is not feasible to compare the performance of different FSMFEHs solely based on load power. Hence, a straightforward approach is to compare their power densities. However, power density also struggles to reflect the performance differences between different FSMFEHs, for reasons analyzed below. Based on the analysis in Section II, the load power P_L satisfies the following relationship with the external magnetic field and dimensions

$$P_L \propto B_{\text{ex}}^2 \cdot f^2 \cdot L^{k1} \cdot R^{k2} (k1 > 0, k2 > 0). \qquad (26)$$

The B_{ex} and f terms in (26) are quadratic because the induced voltage V_{ind} of the FSMFEH is directly proportional to B_{ex} and f, as shown in (1), while the coil resistance R_c remains unaffected by B_{ex} and f. Therefore, according to (1) and (4), P_L exhibits a quadratic relationship with B_{ex} and f. However, $k1$ and $k2$ are difficult to determine and are associated with the absolute values of L and R. On one hand, the effective permeability of the core exhibits a nonlinear relationship with L and R. On the other hand, L and R influence the induced voltage and coil resistance by determining the space used to wind the coil, both of which are impacted by the absolute values of L and R. Therefore, there is a complex nonlinear relationship between load power P_L and L, R, leading to power density D_p being influenced by the absolute values of L and R. In other words, it is challenging to directly quantify the impact of core dimensions on maximum P_L and D_p due to their complex nonlinear relationships with L and R. For FSMFEHs with varying dimensions, even when subjected to the same external magnetic field and utilizing the same performance optimization method, there may still be significant discrepancies in power density.

Based on the above-mentioned analysis, to verify the effectiveness of the performance optimization method in this work, the optimization process and performance comparison should be conducted under the same external magnetic field and dimension conditions. Thus, for each existing study in Table II, we optimized the FSMFEH under the same external magnetic field and dimension conditions as those in the original studies. The optimized load power P_L and power density D_p are then compared with the original results. As evident from Table II, the maximum P_L and D_p decrease when the rectifier losses are considered. Despite this, compared to the original results in existing studies, the optimized maximum P_L increases by 1.43 to 10.2 times, and the optimized maximum D_p increases by 3.02–15.1 times. Furthermore, it is necessary not only to maximize P_L and D_p but also to consider the operating voltage requirements of the power management circuit during the optimization process. During the actual design process, the mathematical model in this work can be used for quantitative analysis of these impact.

V. CONCLUSION

This work accurately estimates the effective permeability of the H-shaped core based on the effective permeability of the cylindrical core and flux continuity theorem, combined with a fitted correction term. A mathematical model for the FSMFEH is established based on the accurately estimated effective permeability. Subsequently, the optimal core and coil parameters are determined utilizing this model, and the performance optimization procedure for the FSMFEH is summarized. In particular, during the optimization process, consideration should be given to the differences between maximum power and maximum power density, as well as the mutual interactions between the FSMFEH and its power management circuit. Combined with the Steinmetz equation, it is concluded that the secondary magnetic field generated by the coil current is the primary factor contributing to core losses. The mathematical model and optimization procedure proposed in this work provide a universal design tool for the FSMFEHs with different external magnetic fields and dimensions, significantly reducing the time and difficulty of design. In addition, to evaluate the effectiveness of different performance optimization methods for the FSMFEH, the optimization process and performance comparison should be carried out under the same external magnetic field and dimension conditions. By applying the proposed model and performance optimization method to existing studies, the maximum power density is increased by 3.02–15.1 times compared with the original results with the same external magnetic field and dimensions.

The magnetic field generated by the coil may induce eddy current losses in surrounding structures (such as busbars, railway tracks, etc.), thereby affecting the coil resistance in the equivalent circuit. For future research, we will focus on developing the mathematical model of the FSMFEH that is coupled with the installation environment. In addition, the output of the FSMFEH must undergo power management stages, such as rectification, maximum power point tracking, energy storage, and dc–dc conversion, before it can power sensors. The circuit design also needs to take into account overvoltage protection and low-power consumption. We will commit to the collaborative design of the FSMFEH and power management circuit to achieve stable and reliable power supply for sensors. The mathematical model and parameter optimization principles of the FSMFEH proposed in this work are expected to provide a universal design tool and guidance for this collaborative design process.

REFERENCES

[1] V. C. Gungor, B. Lu, and G. P. Hancke, “Opportunities and challenges of wireless sensor networks in smart grid,” *IEEE Trans. Ind. Electron.*, vol. 57, no. 10, pp. 3557–3564, Oct. 2010.

[2] J. Chu et al., “Method of sieving the optimal NO_2 sensitive material,” *Sensors Actuators B, Chem.*, vol. 375, 2023, Art. no. 131919.

[3] Q. Wang et al., “Real-time monitoring of air discharge in a switchgear by an intelligent NO_2 sensor module,” *ACS Sensors*, vol. 8, no. 12, pp. 4646–4654, 2023.

[4] K. Ye et al., “A novel method of maximum power point reaching for magnetic field energy harvesting based on a low-power analog control circuit,” *IEEE Trans. Power Electron.*, vol. 39, no. 1, pp. 1888–1897, Jan. 2024.

[5] Y. Li, Y. Yan, H. Yan, J. Hu, and Z. He, “A reconfigurable rectifier-based power improving method of free-standing two-coil magnetic field energy harvesters over a wide load range,” *IEEE Trans. Power Electron.*, vol. 38, no. 5, pp. 5638–5643, May 2023.

[6] P. K. Bonthagorla and S. Mikkili, “A novel fixed PV array configuration for harvesting maximum power from shaded modules by reducing the number of cross-ties,” *IEEE J. Emerg. Sel. Top. Power Electron.*, vol. 9, no. 2, pp. 2109–2121, Apr. 2021.

[7] K. Wang, W. Xia, J. Ren, W. Yu, H. Feng, and S. Hu, “Wind energy harvesting inspired by Palm leaf flutter: Observation, mechanism and experiment,” *Energy Convers. Manage.*, vol. 284, 2023, Art. no. 116971.

[8] Y. Li, Y. Wang, Q. Cao, J. Cao, and D. Qiao, “A self-powered vibration sensor with wide bandwidth,” *IEEE Trans. Ind. Electron.*, vol. 67, no. 1, pp. 560–568, Jan. 2020.

[9] G. Saini, L. Somappa, and M. S. Baghini, “A 500-nW-to-1-mW input power inductive boost converter with MPPT for RF energy harvesting system,” *IEEE J. Emerg. Sel. Top. Power Electron.*, vol. 9, no. 5, pp. 5261–5271, Oct. 2021.

[10] J. W. Jo et al., “A design of boost converter with time-domain MPPT and digital self-tracking ZCD for thermoelectric energy harvesting applications,” *IEEE Trans. Power Electron.*, vol. 38, no. 11, pp. 14226–14235, Nov. 2023.

[11] X. Zeng, Z. Yang, P. Wu, L. Cao, and Y. Luo, “Power source based on electric field energy harvesting for monitoring devices of high-voltage transmission line,” *IEEE Trans. Ind. Electron.*, vol. 68, no. 8, pp. 7083–7092, Aug. 2021.

[12] W. Wang, C. Xu, C. Zhang, and C. Chen, “Start-up and saturation optimization of high-power energy harvester with compound topologies overhead AC transmission line,” *IEEE J. Emerg. Sel. Top. Power Electron.*, vol. 8, no. 4, pp. 3609–3617, Dec. 2020.

[13] M. Gao, L. Yi, and J. Moon, “Mathematical modeling and validation of saturating and clampable cascaded magnetics for magnetic energy harvesting,” *IEEE Trans. Power Electron.*, vol. 38, no. 3, pp. 3455–3468, Mar. 2023.

[14] D. Monagle, E. Ponce, and S. B. Leeb, “Generalized analysis method for magnetic energy harvesters,” *IEEE Trans. Power Electron.*, vol. 37, no. 12, pp. 15764–15773, Dec. 2022.

[15] J. Moon and S. B. Leeb, “Analysis model for magnetic energy harvesters,” *IEEE Trans. Power Electron.*, vol. 30, no. 8, pp. 4302–4311, Aug. 2015.

[16] Y. Zhuang et al., “Improving current transformer-based energy extraction from AC power lines by manipulating magnetic field,” *IEEE Trans. Ind. Electron.*, vol. 67, no. 11, pp. 9471–9479, Nov. 2020.

[17] Z. Liu et al., “A novel method for magnetic energy harvesting based on capacitive energy storage and core saturation modulation,” *IEEE Trans. Ind. Electron.*, vol. 70, no. 3, pp. 2586–2595, Mar. 2023.

[18] S. Paul and J. Chang, “Design of novel electromagnetic energy harvester to power a deicing robot and monitoring sensors for transmission lines,” *Energy Conv. Manage.*, vol. 197, 2019, Art. no. 111868.

[19] Y. Kuang et al., “Magnetic field energy harvesting from the traction return current in rail tracks,” *Appl. Energy*, vol. 292, 2021, Art. no. 116911.

[20] H. Yang, Y. Li, Y. Yan, H. Luo, and Z. He, “A magnetic flux collection enhanced arc-shaped core and its optimal coil turn design method of free-standing magnetic field energy harvester,” *IEEE Trans. Power Electron.*, vol. 38, no. 11, pp. 13567–13572, Nov. 2023.

[21] C. Xu, W. Wang, W. Su, M. Duan, and M. Hu, “Sensitivity analysis of free-standing columnar magnetic field energy harvester for powering wireless monitoring sensors,” *IEEE Trans. Circuits Syst. I, Reg. Papers*, vol. 70, no. 11, pp. 4650–4659, Nov. 2023.

[22] S. Yuan, Y. Huang, J. Zhou, Q. Xu, C. Song, and G. Yuan, “A high-efficiency helical core for magnetic field energy harvesting,” *IEEE Trans. Power Electron.*, vol. 32, no. 7, pp. 5365–5376, Jul. 2017.

[23] A. E. Espe, T. S. Haugan, and G. Mathisen, “Magnetic field energy harvesting in railway,” *IEEE Trans. Power Electron.*, vol. 37, no. 7, pp. 8659–8668, Jul. 2022.

[24] N. M. Roscoe and M. D. Judd, “Harvesting energy from magnetic fields to power condition monitoring sensors,” *IEEE Sensors J.*, vol. 13, no. 6, pp. 2263–2270, Jun. 2013.

[25] S. Yuan, Y. Huang, J. Zhou, Q. Xu, C. Song, and P. Thompson, “Magnetic field energy harvesting under overhead power lines,” *IEEE Trans. Power Electron.*, vol. 30, no. 11, pp. 6191–6202, Nov. 2015.

[26] H. Yang, Y. Li, Z. Liu, H. Luo, Y. Yan, and Z. He, “An accurate power model and high power density design method of free-standing magnetic field energy harvesters with H-shaped core,” *IEEE Trans. Ind. Electron.*, vol. 70, no. 8, pp. 7965–7975, Aug. 2023.

[27] M. E. Kiziroglou, S. W. Wright, and E. M. Yeatman, “Coil and core design for inductive energy receivers,” *Sensors Actuators A, Phys.*, vol. 313, 2020, Art. no. 112206.

[28] M. E. Kiziroglou, S. W. Wright, and E. M. Yeatman, “Power supply based on inductive harvesting from structural currents,” *IEEE Internet Things J.*, vol. 9, no. 10, pp. 7166–7177, May 2022.

[29] Z. Liu et al., “Mathematical modeling and optimization for the power density of the free-standing magnetic field energy harvester,” *IEEE Trans. Power Electron.*, vol. 39, no. 5, pp. 6421–6432, May 2024.

[30] K. Stoyka, G. D. Capua, and N. Femia, “A novel AC power loss model for ferrite power inductors,” *IEEE Trans. Power Electron.*, vol. 34, no. 3, pp. 2680–2692, Mar. 2019.

Zhu Liu received the B.S. degree in electrical engineering, in 2020, from Xi’an Jiaotong University, Xi’an, China, where he is currently working toward the Ph.D. degree in electrical engineering with the Department of Electrical Engineering.

His main research interests include magnetic energy harvesting and power management circuit.

Likai Zheng received the B.S. degree in electrical engineering, in 2023, from the School of Electrical Engineering, Xi’an Jiaotong University, Xi’an, China, where he is currently working toward the master’s degree in electrical engineering with the Department of Electrical Engineering.

His main research interests include magnetic energy harvesting and power management.

Siyu Bao received the B.S. degree in electrical engineering from Northeastern University, Shenyang, China, in 2022. She is currently working toward the master’s degree in electrical engineering from Xi’an Jiaotong University, Xi’an, China.

Her main research interests focuses on magnetic field energy harvesting.

Aijun Yang (Senior Member, IEEE) received the B.S. and Ph.D. degrees in electrical engineering from Xi’an Jiaotong University, Xi’an, China, in 2009 and 2014, respectively.

He is currently a Professor with Xi’an Jiaotong University. His main research interests include condition monitoring technique, energy harvesters, and fault diagnosis.

Dan Zhou received the B.S. and Ph.D. degrees in electrical engineering from North China Electric Power University, Beijing, China, in 2007 and 2013, respectively.

She is currently a Senior Engineer with the Electric Power Research Institute of Guangdong Power Grid Company, Ltd., Guangzhou, China. Her research interests include high voltage testing, condition monitoring, and maintenance management of substation equipment.

Jifeng Chu received the B.S. degree in electrical engineering from Southwest Jiaotong University, Chengdu, China, in 2016, and the Ph.D. degree in electrical engineering from the College of Electrical Engineering of Xi’an Jiaotong University, Xi’an, China, in 2021.

He is currently doing Postdoctoral Research with Xi’an Jiaotong University. His main research interests include the application of gas sensors and artificial intelligence in power equipment.

Huan Yuan received the B.S. degree in electrical engineering from Southwest Jiaotong University, Chengdu, China, in 2014, and the Ph.D. degree in electrical engineering from Xi’an Jiaotong University, Xi’an, China, in 2019.

He is currently an Associate Professor with Xi’an Jiaotong University. His main research interests include energy harvesting, wireless power transfer, fault diagnosis, and artificial intelligence.

Mingzhe Rong (Senior Member, IEEE) received the B.S. and Ph.D. degrees in electrical engineering from Xi’an Jiaotong University, Xi’an, China, in 1984 and 1990, respectively.

He is currently a Professor with Xi’an Jiaotong University. He research interests include the detection and diagnosis techniques for electrical equipment, on-line monitoring technique. He is an IET Fellow.

Xiaohua Wang (Senior Member, IEEE) received the B.S. degree in electrical engineering from Chang’an University, Xi’an, China, in 2000, and the Ph.D. degree in electrical engineering from Xi’an Jiaotong University, Xi’an, China, in 2006.

He is currently a Professor with Xi’an Jiaotong University. His main research interests include condition monitoring technique, fault diagnosis, energy harvesters, and artificial intelligence.